

# Experimental realization of the topological Haldane model with ultracold fermions

Gregor Jotzu<sup>1</sup>, Michael Messer<sup>1</sup>, Rémi Desbuquois<sup>1</sup>, Martin Lebrat<sup>1</sup>, Thomas Uehlinger<sup>1</sup>, Daniel Greif<sup>1</sup> & Tilman Esslinger<sup>1</sup>

The Haldane model on a honeycomb lattice is a paradigmatic example of a Hamiltonian featuring topologically distinct phases of matter<sup>1</sup>. It describes a mechanism through which a quantum Hall effect can appear as an intrinsic property of a band structure, rather than being caused by an external magnetic field<sup>2</sup>. Although physical implementation has been considered unlikely, the Haldane model has provided the conceptual basis for theoretical and experimental research exploring topological insulators and superconductors<sup>2–6</sup>. Here we report the experimental realization of the Haldane model and the characterization of its topological band structure, using ultracold fermionic atoms in a periodically modulated optical honeycomb lattice. The Haldane model is based on breaking both time-reversal symmetry and inversion symmetry. To break time-reversal symmetry, we introduce complex next-nearest-neighbour tunnelling terms, which we induce through circular modulation of the lattice position<sup>7</sup>. To break inversion symmetry, we create an energy offset between neighbouring sites<sup>8</sup>. Breaking either of these symmetries opens a gap in the band structure, which we probe using momentum-resolved interband transitions. We explore the resulting Berry curvatures, which characterize the topology of the lowest band, by applying a constant force to the atoms and find orthogonal drifts analogous to a Hall current. The competition between the two broken symmetries gives rise to a transition between topologically distinct regimes. By identifying the vanishing gap at a single Dirac point, we map out this transition line experimentally and quantitatively compare it to calculations using Floquet theory without free parameters. We verify that our approach, which allows us to tune the topological properties dynamically, is suitable even for interacting fermionic systems. Furthermore, we propose a direct extension to realize spin-dependent topological Hamiltonians.

In a honeycomb lattice that is symmetric under time-reversal and inversion, the two lowest bands are connected at two Dirac points. Each broken symmetry leads to a gapped energy spectrum. F. D. M. Haldane realized that the resulting phases are topologically distinct<sup>1</sup>: A broken inversion symmetry (IS), caused by an energy offset between the two sublattices, leads to a trivial band insulator at half-filled lattice sites. Time-reversal symmetry (TRS) can be broken by complex next-nearest-neighbour tunnel couplings (Fig. 1a). The corresponding staggered magnetic fluxes sum up to zero in one unit cell, thereby preserving the translation symmetry of the lattice. This gives rise to a topological Chern insulator, where a non-zero Hall conductance appears despite the absence of a net magnetic field<sup>1,2</sup>. When both symmetries are broken, a topological phase transition connects two regimes with a distinct topological invariant, the Chern number, which changes from 0 to +1 or to −1; see Fig. 1b. There, the gap closes at a single Dirac point. These transitions have attracted great interest because they cannot be described by Landau's theory of phase transitions, owing to the absence of a changing local order parameter<sup>6</sup>.

A crucial experimental challenge for the realization of the Haldane model is the creation of complex next-nearest-neighbour tunnelling. Here we show that this is possible with ultracold atoms in optical lattices periodically modulated in time. Pioneering experiments with bosons showed a renormalization of existing tunnelling amplitudes in one dimension<sup>9,10</sup>, and were extended to control tunnelling phases<sup>11,12</sup> and higher-order

tunnelling<sup>13</sup>. In higher dimensions this allowed the study of phase transitions<sup>14,15</sup>, and topologically trivial staggered fluxes were realized<sup>16,17</sup>. Furthermore, uniform flux configurations were observed using rotation and laser-assisted tunnelling<sup>18,19</sup>, although for the latter method, heating seemed to prevent the observation of a flux in some experiments<sup>20</sup>. In a honeycomb lattice, a rotating force, as proposed by T. Oka and H. Aoki, can induce the required complex tunnelling<sup>7</sup>. Using arrays of coupled waveguides, a classical version of this proposal was used to study topologically protected edge modes in the inversion-symmetric regime<sup>21</sup>. We

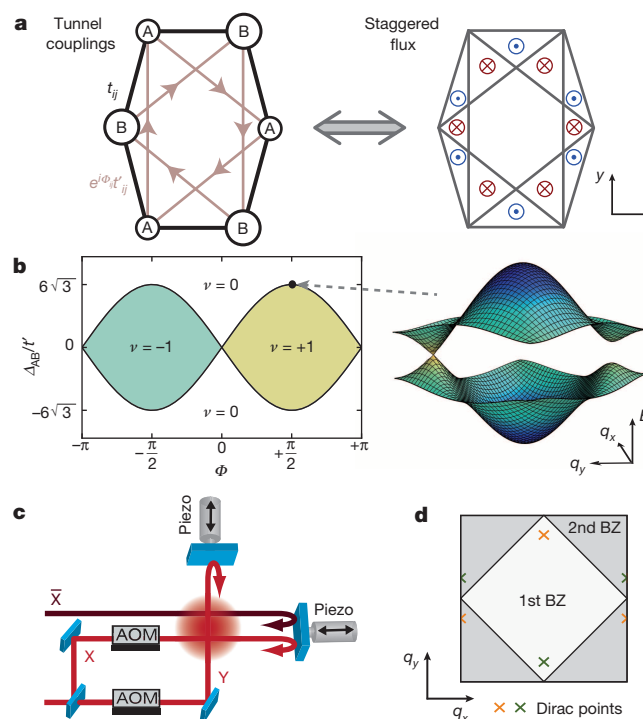


**Figure 1 | The Haldane model.** **a**, Tight-binding model of the honeycomb lattice realized in the experiment. An energy offset  $\Delta_{AB}$  between sublattice A and B breaks IS. Nearest-neighbour tunnel couplings  $t_{ij}$  have real values, whereas next-nearest-neighbour tunnelling  $e^{i\phi_{ij}}t'_{ij}$  carries tunable phases indicated by arrows.  $i$  and  $j$  indicate the indices of the connected lattice sites. For a detailed discussion of anisotropies and higher-order tunnelling terms, see the Supplementary Information. The corresponding staggered magnetic fluxes (sketched on the right) sum up to zero but break TRS. **b**, Topological regimes of the Haldane model, for isotropic  $t_{ij}$ ,  $t'_{ij} = t'$  and  $\Phi_{ij} = \Phi$ . The trivial (Chern number  $\nu = 0$ ) and Chern-insulating ( $\nu = \pm 1$ ) regimes are connected by topological transitions (black lines), where the band structure (shown on the right) becomes gapless at a single Dirac point. **c**, Laser beam set-up forming the optical lattice. The laser  $\bar{X}$  is frequency-detuned from the other beams. Piezo-electric actuators sinusoidally modulate the retro-reflecting mirrors, with a controllable phase difference  $\phi$ . Acousto-optic modulators (AOMs) ensure the stability of the lattice geometry (Methods). **d**, The resulting Brillouin zones (BZ), featuring two Dirac points in quasi-momentum space  $\mathbf{q}$ .

<sup>1</sup>Institute for Quantum Electronics, ETH Zurich, 8093 Zurich, Switzerland.

access the full parameter space of the Haldane model using a fermionic quantum gas, by extending the proposal to elliptical modulation of the lattice position and additionally breaking IS through a deformation of the lattice geometry.

The starting point of our experiment is a non-interacting, ultracold gas of  $4 \times 10^4$  to  $6 \times 10^4$  fermionic  $^{40}\text{K}$  atoms prepared in the lowest band of a honeycomb optical lattice created by several laser beams at wavelength  $\lambda = 1,064$  nm, arranged in the  $x$ - $y$  plane as depicted in Fig. 1c and detailed in ref. 8. The two lowest bands have a total bandwidth of  $h \times 3.9(1)$  kHz (where  $h$  is Planck's constant), with a gap of  $h \times 5.4(2)$  kHz to the next higher band, and contain two Dirac points at opposite quasi-momenta; see Fig. 1d. After loading the atoms into the honeycomb lattice, we ramp up a sinusoidal modulation of the lattice position along the  $x$  and  $y$  directions with a final amplitude of  $0.087(1)\lambda$ , frequency 4.0 kHz and phase difference  $\varphi$ . This gives access to linear ( $\varphi = 0^\circ$  or  $180^\circ$ ), circular ( $\varphi = \pm 90^\circ$ ) and elliptical trajectories.

The effective Hamiltonian of our system in the phase-modulated honeycomb lattice is computed using analytical and numerical Floquet theory (see the Methods and Supplementary Information for a detailed discussion). It is well described by the Haldane model<sup>1</sup>

$$\hat{H} = \sum_{\langle ij \rangle} t_{ij} \hat{c}_i^\dagger \hat{c}_j + \sum_{\langle\langle ij \rangle\rangle} e^{i\Phi_{ij}} t'_{ij} \hat{c}_i^\dagger \hat{c}_j + \Delta_{AB} \sum_{i \in A} \hat{c}_i^\dagger \hat{c}_i \quad (1)$$

where  $t_{ij}$  and  $t'_{ij}$  are real-valued nearest- and next-nearest-neighbour tunnelling amplitudes, and the latter contain additional phases  $\Phi_{ij}$  defined along the arrows shown in Fig. 1a. The fermionic creation and annihilation operators are denoted by  $\hat{c}_i^\dagger$  and  $\hat{c}_i$ . The energy offset  $\Delta_{AB} \geq 0$  between sites of the  $A$  and  $B$  sublattice breaks IS and opens a gap  $|\Delta_{AB}|$  (ref. 8). TRS can be broken by changing  $\varphi$ . This controls the imaginary part of the next-nearest-neighbour tunnelling, whereas its real part, as well as  $t_{ij}$  and  $\Delta_{AB}$ , are mostly unaffected (Methods). Breaking only TRS opens an energy gap  $|\Delta_T|$  at the Dirac points, given by a sum of the imaginary part of the three next-nearest-neighbour tunnel couplings connecting the same sublattice

$$\Delta_T = - \sum_i w_i t'_i \sin(\Phi_i) = \Delta_T^{\max} \sin(\varphi) \quad (2)$$

with weights  $w_i$  of order unity, which depend on the position of the Dirac points in the Brillouin zone. The sum is taken over the different types of next-nearest-neighbour bond, and the origin of the second equality is discussed in the Supplementary Information. Circular modulation ( $\varphi = \pm 90^\circ$ ) leads to a maximum gap ( $h \times 88^{+10}_{-34}$  Hz for our parameters), whereas the gap vanishes for linear modulation ( $\varphi = 0^\circ, \pm 180^\circ$ ), where TRS is preserved.

We will first present measurements which confirm that breaking either symmetry is sufficient to open a gap in the band structure. For this, we restrict ourselves to either  $\varphi = 0^\circ$  or  $\Delta_{AB} = 0$ , corresponding to the two axes of the Haldane diagram of Fig. 1b. Subsequently we will present measurements in which we explore the topology of the lowest band in the same parameter regime by probing the Berry curvature. To probe the opening of gaps in the system, we drive Landau-Zener transitions through the Dirac points<sup>8,22</sup>. Applying a constant force along the  $x$  direction by means of a magnetic field gradient causes an energy offset  $\Delta E/h = 103.6(1)$  Hz per site, thereby inducing a Bloch oscillation. After one full Bloch cycle the gradient is removed and the fraction of atoms  $\xi$  in the second band is determined using a band-mapping procedure (Methods). For broken IS, a gap given by  $|\Delta_{AB}|$  opens at both Dirac points. In this case,  $\xi$  reaches a maximum at  $\Delta_{AB} = 0$ , which indicates a vanishing energy gap, and decays symmetrically around this point as expected; see Fig. 2a. In the case of broken TRS (Fig. 2b), a reduction in transfer versus modulation phase is observed. This signals an opening gap, which is found to be largest for circular modulation, as expected from equation (2).

Breaking either IS or TRS gives rise to similar, gapped band structures which remain point-symmetric around quasi-momentum  $\mathbf{q} = 0$ . However, the energy spectrum itself is not sufficient to reveal the different topology of the band, which is given by the associated eigenstates. These are characterized by a local geometrical property: the Berry curvature  $\Omega(\mathbf{q})$  (ref. 6). In  $\mathbf{q}$ -space,  $\Omega(\mathbf{q})$  is analogous to a magnetic field and corresponds

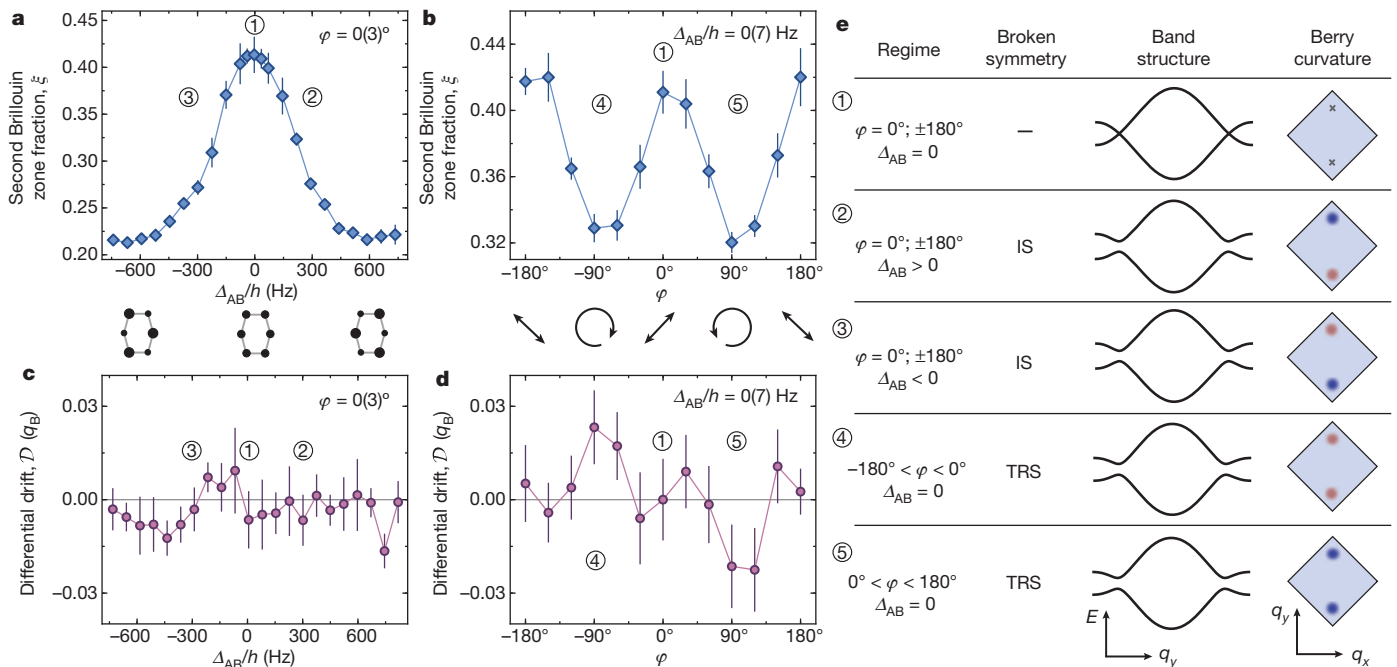


**Figure 2 | Probing gaps and Berry curvature.** **a, b**, Fraction of atoms in the second band  $\xi$  after one Bloch oscillation in the  $q_x$  direction. We break either IS (**a**) by introducing a sublattice offset  $\Delta_{AB}$  or TRS (**b**) via elliptical modulation (see diagrams below). This corresponds to scanning either of the two axes of the Haldane model. A gap opens at both Dirac points, given by  $|\Delta_{AB}|$  or  $|\Delta_T^{\max} \sin(\varphi)|$ , respectively, thereby reducing  $\xi$ . **c, d**, Differential drift  $\mathcal{D}$  obtained from Bloch oscillations in opposite  $q_y$  directions. For broken IS (**c**),

the opposite Berry curvatures at the two Dirac points cancel each other, while for broken TRS (**d**) the system enters the topological regime, where opposite drifts for  $\varphi \geq 0$  are expected. Data show mean  $\pm$  s.d. of at least 6 (**a–c**) or 21 (**d**) measurements, and the Bloch momentum  $q_B = 2\pi/\lambda$ . The numbers in parentheses are the standard deviations of the calibrations of the parameters used for those plots. **e**, Sketches illustrating gaps and Berry curvature in different regimes. Red (blue) indicates positive (negative) Berry curvature.

to the geometric phase picked up along an infinitesimal loop. When only IS is broken, the Berry curvature is point-antisymmetric, and its sign inverts for opposite  $\Delta_{AB}$ ; see Fig. 2e. The spread of  $\Omega(\mathbf{q})$  increases with the size of the gap. Its integral over the first Brillouin zone, the Chern number  $\nu$ , is zero, corresponding to a topologically trivial system. However, with only TRS broken,  $\nu = \pm 1$ ,  $\Omega(\mathbf{q})$  is point-symmetric, and its sign changes when reversing the rotation direction of the lattice modulation.

To determine the topology of the lowest band, we move the atoms along the  $y$  direction such that their trajectories sample the regions where the Berry curvature is concentrated, and record their final position. As atoms move through regions of  $\mathbf{q}$ -space with non-zero curvature, they acquire an orthogonal velocity proportional to the applied force and  $\Omega(\mathbf{q})$  (refs 23–26). The underlying harmonic confinement caused by the laser beams in the experiment couples real and momentum space, meaning that a displacement in real space leads to a drift in quasi-momentum. We apply a gradient of  $\Delta E/\hbar = 114.6(1)$  Hz per site and measure the centre of mass of the quasi-momentum distribution in the lowest band after one full Bloch cycle. Because the velocity caused by the Berry curvature inverts when inverting the force, we subtract the result for the opposite gradient to obtain the differential drift  $\mathcal{D}$ . This quantity is more suitable for distinguishing trivial from non-trivial Berry-curvature distributions than the response to a single gradient (Methods)<sup>25</sup>. The latter does however provide information about the local Berry curvature and is shown in Extended Data Fig. 2.

When breaking only IS, we observe that  $\mathcal{D}$  vanishes and is independent of  $\Delta_{AB}$ , because the Berry curvature is point-antisymmetric; see Fig. 2c. In contrast, when only TRS is broken, we explore the topological regime of the Haldane model with  $\Delta_{AB} = 0$ . A differential drift is observed for  $\varphi = 90^\circ$ , which, as expected, is opposite for  $\varphi = -90^\circ$ ; see Figs 2d and 4c. This is a direct consequence of the Berry curvature being point-symmetric, with its sign given by the rotation direction of the lattice modulation. In fact, here a non-zero  $\mathcal{D}$  can only originate from a non-zero integrated Berry curvature (Methods). As the modulation becomes linear, the drift disappears. This is smoothed by the increased transfer to the higher band when the gap becomes smaller, which predominantly affects atoms that would experience the strongest Berry curvature. These observations are qualitatively confirmed by semiclassical simulations shown in Extended Data Fig. 1.

Within the Haldane model, the competition of simultaneously broken TRS and IS is of particular interest, as it features a topological transition between a trivial band insulator and a Chern insulator. In this regime, both the band structure and Berry curvature are no longer point-symmetric and the energy gap  $G_\pm$  at the two Dirac points is given by

$$G_\pm = |\Delta_{AB} \pm \Delta_T^{\max} \sin(\varphi)| \quad (3)$$

On the transition lines the system is gapless with one closed and one gapped Dirac point,  $G_+ = 0$  or  $G_- = 0$ . We now discuss measurements in which we extend the parameter regime to allow for the simultaneous breaking of both symmetries.

We map out the transition by measuring the transfer  $\xi_\pm$  for each Dirac point separately, see Fig. 3a.  $\xi_+$  ( $\xi_-$ ) is the fraction of atoms occupying the upper (lower) half of the second Brillouin zone after one Bloch oscillation along the  $x$  direction. We observe a difference between  $\xi_+$  and  $\xi_-$ , which shows that the band structure is no longer point-symmetric, allowing for the parity anomaly predicted by Haldane<sup>1</sup>. When the topology of the band changes, the gap at one of the Dirac point closes. We identify the closing of a gap with the point of maximum measured transfer when varying  $\Delta_{AB}$ . For  $\varphi = 0^\circ$  we find, as expected for preserved TRS, that the maxima of both  $\xi_+$  and  $\xi_-$  coincide; see Fig. 3b. The maxima are shifted in opposite directions for  $\varphi = 90^\circ$ , showing that the minimum gap for each Dirac point occurs at different values of  $\Delta_{AB}$ . In between these values the system is in the topologically non-trivial regime. We explore the position of each maximum for varying  $\varphi$  and find opposite shifts for negative  $\varphi$  as predicted by equation (3) using no free parameters; see Fig. 3c.

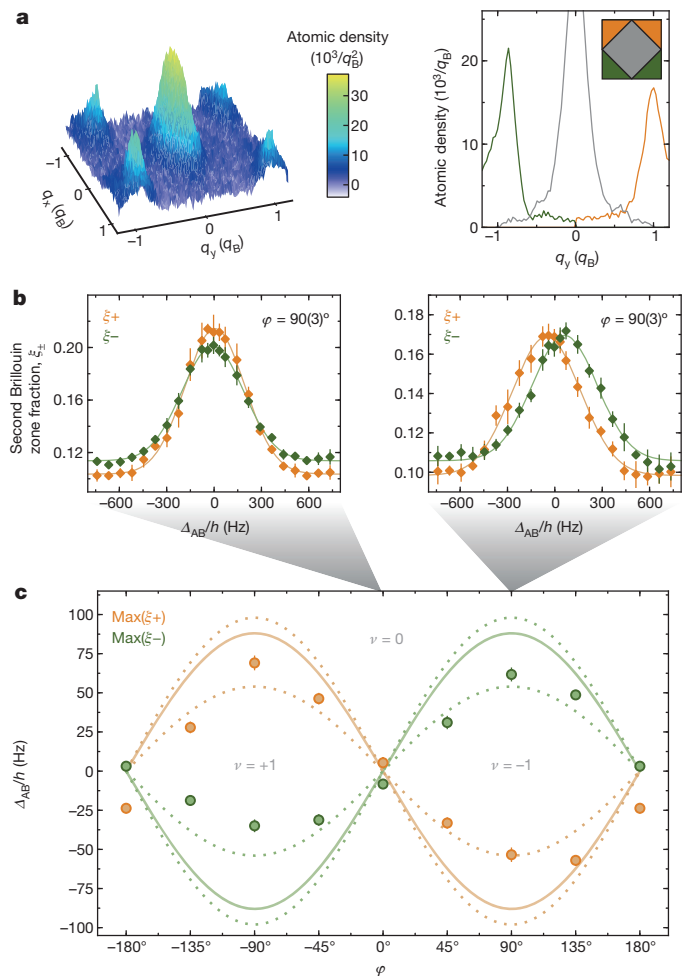


**Figure 3 | Mapping out the transition line.** **a**, Atomic quasi-momentum distribution (averaged over six runs) after one Bloch oscillation for  $\varphi = +90^\circ$ ,  $\Delta_{AB}/h = 292(7)$  Hz. A line sum along  $q_x$  shows the atomic density in the first Brillouin zone in grey; atoms transferred at the upper (lower) Dirac point are shown in orange (green) throughout. The fraction of atoms in the second Brillouin zone differs for  $q_y \gtrless 0$ . This is a direct consequence of simultaneously broken IS and TRS, which allows band structures that are not point-symmetric. **b**, Fractions of atoms  $\xi_\pm$  in each half of the second Brillouin zone. For linear modulation (left) the gap vanishes at  $\Delta_{AB} = 0$  for both Dirac points, while for circular modulation (right) it vanishes at opposite values of  $\Delta_{AB}$ . Gaussian fits (solid lines) are used to find the maximum transfer, which signals the topological transition. Data are mean  $\pm$  s.d. of at least six measurements. **c**, Solid lines show the theoretically computed topological transitions, without free parameters. Dotted lines represent the uncertainty of the maximum gap  $|\Delta_T^{\max}|/h = 88^{+10}_{-34}$  Hz, originating from the uncertainty of the lattice parameters. Data are the points of maximum transfer for each Dirac point,  $\pm$  the fitting error, obtained from measurements as in **b** for various  $\varphi$ . Data points for  $\varphi = \pm 180^\circ$  correspond to the same measurements. Between the lines, the system is in the topologically non-trivial regime.

In Fig. 4 we show the measured differential drift  $\mathcal{D}$  for all topological regimes, allowing for simultaneously broken IS and TRS. Here, we reduce the modulation frequency to 3.75 kHz, where the signal-to-noise ratio of  $\mathcal{D}$  is larger, but which is less suited for a quantitative comparison of the transfer  $\xi$  because the lattice modulation ramps are expected to be less adiabatic.  $\mathcal{D}$  is non-zero only for broken TRS and shows the expected antisymmetry with  $\varphi$  and symmetry with  $\Delta_{AB}$ . For large  $\Delta_{AB}$ , deep inside the topologically trivial regime,  $\mathcal{D}$  vanishes for all  $\varphi$ . For smaller  $\Delta_{AB}$ , the differential drift shows precursors of the regimes with non-zero Chern number: non-zero values of  $\mathcal{D}$  extend well beyond the transition lines when IS and TRS are both broken. Semiclassical simulations (see Extended Data Fig. 1c) suggest that the main contribution to this effect arises from the transfer to the higher band.



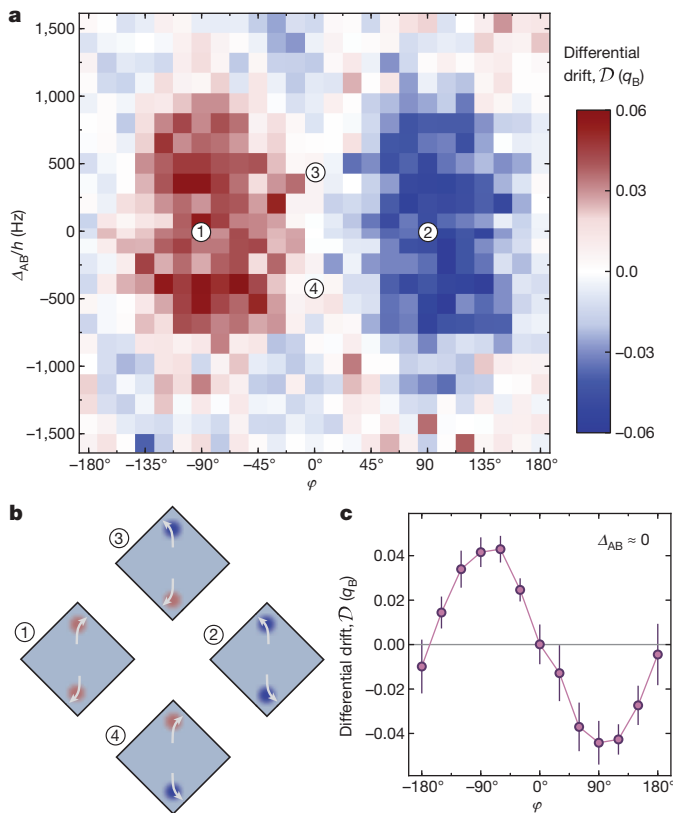


**Figure 4 | Drift measurements.** **a**, Differential drift  $\mathcal{D}$  in quasi-momentum. Each pixel corresponds to at least one pair of measurements, where the modulation frequency was set to 3.75 kHz. Data points for  $\varphi = \pm 120^\circ$ ,  $\Delta_{AB}/h = 503(7)$  Hz were not recorded and are interpolated. **b**, All topological regimes are explored and the expected momentum-space drifts caused by the Berry curvature are sketched for selected parameters. **c**, Cut along the  $\Delta_{AB}/h = 15(7)$  Hz line. Data show mean  $\pm$  s.d. for at least six pairs of measurements.

Extending our work to interacting systems requires sufficiently low heating. We investigate this with a repulsively interacting spin mixture in the honeycomb lattice previously used for studying the fermionic Mott insulator<sup>27</sup>. We measure the entropy in the Mott insulating regime by loading atoms into the lattice and reversing the loading procedure (see Methods and Extended Data Fig. 3). The entropy increase is only 25% larger than without modulation. This opens up the possibility of studying topological models with interactions<sup>28</sup> in a controlled and tunable way. For example, lattice modulation could be used to create topological flat bands, which have been suggested to give rise to interaction-induced fractional Chern insulators<sup>29,30</sup>. Furthermore, our approach of periodically modulating the system can be directly extended to engineer Hamiltonians with spin-dependent tunnelling amplitudes and phases (Methods). This can be achieved by modulating a magnetic field gradient, which leads to spin-dependent oscillating forces owing to the differential Zeeman shift. For example, TRS topological Hamiltonians, such as the Kane–Mele model<sup>3</sup>, can be implemented by simultaneously modulating the lattice on one axis and a magnetic field gradient on the other.

**Online Content** Methods, along with any additional Extended Data display items and Source Data, are available in the online version of the paper; references unique to these sections appear only in the online paper.

Received 19 June; accepted 29 September 2014.

- Haldane, F. D. M. Model for a quantum Hall Effect without Landau levels: condensed-matter realization of the ‘parity’ anomaly. *Phys. Rev. Lett.* **61**, 2015–2018 (1988).

- Chang, C.-Z. *et al.* Experimental observation of the quantum anomalous Hall effect in a magnetic topological insulator. *Science* **340**, 167–170 (2013).
- Kane, C. L. & Mele, E. J. Quantum spin Hall effect in graphene. *Phys. Rev. Lett.* **95**, 226801 (2005).
- König, M. *et al.* Quantum spin Hall insulator state in HgTe quantum wells. *Science* **318**, 766–770 (2007).
- Hsieh, D. *et al.* A topological Dirac insulator in a quantum spin Hall phase. *Nature* **452**, 970–974 (2008).
- Hasan, M. Z. & Kane, C. L. Topological insulators. *Rev. Mod. Phys.* **82**, 3045–3067 (2010).
- Oka, T. & Aoki, H. Photovoltaic Hall effect in graphene. *Phys. Rev. B* **79**, 081406 (2009).
- Tarruell, L., Greif, D., Uehlinger, T., Jotzu, G. & Esslinger, T. Creating, moving and merging Dirac points with a Fermi gas in a tunable honeycomb lattice. *Nature* **483**, 302–305 (2012).
- Dunlap, D. & Kenkre, V. Dynamic localization of a charged particle moving under the influence of an electric field. *Phys. Rev. B* **34**, 3625–3633 (1986).
- Lignier, H. *et al.* Dynamical control of matter-wave tunneling in periodic potentials. *Phys. Rev. Lett.* **99**, 220403 (2007).
- Struck, J. *et al.* Tunable gauge potential for neutral and spinless particles in driven optical lattices. *Phys. Rev. Lett.* **108**, 225304 (2012).
- Jiménez-García, K. *et al.* Peierls substitution in an engineered lattice potential. *Phys. Rev. Lett.* **108**, 225303 (2012).
- Parker, C. V., Ha, L.-C. & Chin, C. Direct observation of effective ferromagnetic domains of cold atoms in a shaken optical lattice. *Nature Phys.* **9**, 769–774 (2013).
- Zenesini, A., Lignier, H., Ciampini, D., Morsch, O. & Arimondo, E. Coherent control of dressed matter waves. *Phys. Rev. Lett.* **102**, 100403 (2009).
- Struck, J. *et al.* Quantum simulation of frustrated classical magnetism in triangular optical lattices. *Science* **333**, 996–999 (2011).
- Aidelsburger, M. *et al.* Experimental realization of strong effective magnetic fields in an optical lattice. *Phys. Rev. Lett.* **107**, 255301 (2011).
- Struck, J. *et al.* Engineering Ising-XY spin-models in a triangular lattice using tunable artificial gauge fields. *Nature Phys.* **9**, 738–743 (2013).
- Williams, R. A., Al-Assam, S. & Foot, C. J. Observation of vortex nucleation in a rotating two-dimensional lattice of Bose-Einstein condensates. *Phys. Rev. Lett.* **104**, 050404 (2010).
- Aidelsburger, M. *et al.* Realization of the Hofstadter Hamiltonian with ultracold atoms in optical lattices. *Phys. Rev. Lett.* **111**, 185301 (2013).
- Miyake, H., Siviloglou, G. A., Kennedy, C. J., Burton, W. C. & Ketterle, W. Realizing the Harper Hamiltonian with laser-assisted tunneling in optical lattices. *Phys. Rev. Lett.* **111**, 185302 (2013).
- Rechtsman, M. C. *et al.* Photonic Floquet topological insulators. *Nature* **496**, 196–200 (2013).
- Lim, L.-K., Fuchs, J.-N. & Montambaux, G. Bloch-Zener oscillations across a merging transition of Dirac points. *Phys. Rev. Lett.* **108**, 175303 (2012).
- Chang, M.-C. & Niu, Q. Berry phase, hyperorbits, and the Hofstadter spectrum. *Phys. Rev. Lett.* **75**, 1348–1351 (1995).
- Dudarev, A. M., Diener, R. B., Carusotto, I. & Niu, Q. Spin-orbit coupling and Berry phase with ultracold atoms in 2D optical lattices. *Phys. Rev. Lett.* **92**, 153005 (2004).
- Price, H. M. & Cooper, N. R. Mapping the Berry curvature from semiclassical dynamics in optical lattices. *Phys. Rev. A* **85**, 033620 (2012).
- Dauphin, A. & Goldman, N. Extracting the Chern number from the dynamics of a Fermi gas: implementing a quantum Hall bar for cold atoms. *Phys. Rev. Lett.* **111**, 135302 (2013).
- Uehlinger, T. *et al.* Artificial graphene with tunable interactions. *Phys. Rev. Lett.* **111**, 185307 (2013).
- Varney, C. N., Sun, K., Rigol, M. & Galiatski, V. Interaction effects and quantum phase transitions in topological insulators. *Phys. Rev. B* **82**, 115125 (2010).
- Neupert, T., Santos, L., Chamon, C. & Mudry, C. Fractional quantum Hall states at zero magnetic field. *Phys. Rev. Lett.* **106**, 236804 (2011).
- Grushin, A. G., Gómez-León, A. & Neupert, T. Floquet fractional Chern insulators. *Phys. Rev. Lett.* **112**, 156801 (2014).

**Supplementary Information** is available in the online version of the paper.

**Acknowledgements** We thank H. Aoki for drawing our attention to the relevance of their proposal for optical lattices and N. Cooper, S. Huber, L. Tarruell, L. Wang and A. Zenesini for discussions. We acknowledge the SNF, the NCCR-QSIT and the SQMS (ERC advanced grant) for funding.

**Author Contributions** The data were measured by G.J., M.M., R.D. and D.G. and analysed by G.J., M.M., R.D., T.U. and D.G. The theoretical framework was developed by G.J. and M.L. All work was supervised by T.E. All authors contributed to planning the experiment, discussions and the preparation of the manuscript.

**Author Information** Reprints and permissions information is available at [www.nature.com/reprints](http://www.nature.com/reprints). The authors declare no competing financial interests. Readers are welcome to comment on the online version of the paper. Correspondence and requests for materials should be addressed to T.E. ([esslinger@phys.ethz.ch](mailto:esslinger@phys.ethz.ch)).

## METHODS

**Spin-polarized Fermi gas.** After sympathetic cooling with  $^{87}\text{Rb}$  in a magnetic trap,  $1 \times 10^6$  fermionic  $^{40}\text{K}$  atoms are transferred into an optical dipole trap operating at a wavelength of 826 nm. A balanced spin mixture of the  $|F, m_F\rangle = |9/2, -9/2\rangle$  and  $|9/2, -7/2\rangle$  Zeeman states, where  $F$  denotes the hyperfine manifold and  $m_F$  the magnetic sub-level, is evaporatively cooled at a magnetic field of 197.6(1) G, in the vicinity of the Feshbach resonance located at 202.1 G. We obtain typical temperatures of  $0.2T_F$ , where  $T_F$  is the Fermi temperature. The field is subsequently reduced and a magnetic field gradient is used to selectively remove the  $|9/2, -7/2\rangle$  component, while levitating the atoms in the  $|9/2, -9/2\rangle$  state against gravity.

**Honeycomb optical lattice.** This polarized Fermi gas is loaded into the optical lattice within 200 ms using an S-shaped intensity ramp, and the dipole trap is subsequently turned off in 100 ms. The lattice potential is given by<sup>8</sup>

$$V(x, y, z) = -V_X \cos^2(k_{\text{lat}}x + \theta/2) - V_X \cos^2(k_{\text{lat}}x) \\ - V_Y \cos^2(k_{\text{lat}}y) - 2\alpha\sqrt{V_X V_Y} \cos(k_{\text{lat}}x) \cos(k_{\text{lat}}y) \cos\varphi_L \quad (4) \\ - V_Z \cos^2(k_{\text{lat}}z)$$

where  $V_{X,Y,Z}$  are the single-beam lattice depths and  $k_{\text{lat}} = 2\pi/\lambda$ . Gravity points along the negative  $y$ -direction. To control the energy offset  $\mathcal{A}_{AB}$ , we vary  $\theta$  around  $\pi$  by changing the frequency detuning  $\delta$  between the  $\bar{X}$  and the  $X$  (which has the same frequency as  $Y$ ) beams using an acousto-optic modulator; see Fig. 1c. The point where  $\mathcal{A}_{AB} = 0$  is determined from transfer measurements in a static lattice with an accuracy of 7 Hz. The phase  $\varphi_{\text{lat}}$  is stabilized to  $0.0(3)^\circ$  using a heterodyne interferometer<sup>8</sup>, and the visibility of the interference pattern is  $\alpha = 0.81(1)$ . We minimize the intensity imbalance between the incoming and reflected lattice beams in the  $x$ - $y$  plane such that the remaining imbalance between left and right vertical tunnelling is less than 0.3%, as determined from Raman-Nath diffraction on a  $^{87}\text{Rb}$  Bose-Einstein condensate. The final lattice depths are set to  $V_{X,X,Y,Z} = [5.0(3), 0.45(2), 2.3(1), 0] E_R$ , where the recoil energy  $E_R = \hbar^2/2m\lambda^2$ , and  $m$  denotes the mass of  $^{40}\text{K}$ . Using a Wannier function calculation<sup>27</sup>, we extract the corresponding tight-binding parameters  $t_{0,1,2,3}/\hbar = [-746(81), -527(17), -527(17), -126(7)]$  Hz, for the horizontal, the left and right vertical nearest-neighbour tunnelling links, and the horizontal link across the honeycomb cell, respectively (see Supplementary Information). This results in a bandwidth of  $W/\hbar = 3.9(1)$  kHz. The amplitudes for the next-nearest-neighbour tunnel couplings are  $t'_{1,2,3}/\hbar = [14, 14, 61]$  Hz and do not affect the gaps and the topological transition line. The nearest-neighbour tunnelling is renormalized in the modulated lattice, which decreases the effective bandwidth to  $W_{\text{eff}}/\hbar = 3.3(1)$  kHz.

All experiments are carried out in the presence of a weak underlying harmonic confinement with trapping frequencies  $\omega_{x,y,z}/2\pi = [14.4(6), 30.2(1), 29.3(3)]$  Hz, which originates from the Gaussian intensity profiles of the red-detuned lattice beams. The lattice depths are calibrated using Raman-Nath diffraction on a  $^{87}\text{Rb}$  Bose-Einstein condensate. To determine  $\alpha$ , we drive quasi-momentum resolved inter-band transitions for a spin-polarized Fermi gas loaded into a chequerboard lattice by periodically modulating the lattice depth, and we measure the band gap at  $\mathbf{q} = 0$ . **Modulation of the optical lattice.** The two mirrors used for retro-reflecting the lattice beams are mounted on piezo-electric actuators, which allow for a controlled phase shift of the reflected beams with respect to the incoming lattice beams. To fix the geometry of the lattice, the relative phase  $\varphi_{\text{lat}}$  of the two orthogonal retro-reflected beams  $X$  and  $Y$  is actively stabilized to  $\varphi_{\text{lat}} = 0^\circ$ . To maintain this phase relation during modulation, the phase of the respective incoming beams is modulated at the same frequency as the piezo-electric actuators using acousto-optical modulators. In addition, this phase modulation provides a direct calibration of the amplitude and relative phase of the mirror displacement. The calibration is confirmed by measuring both the reduction of tunnelling<sup>10</sup> and the effective atomic mass around  $\mathbf{q} = 0$  in a modulated simple cubic lattice.

The modulation is turned on as follows: the atoms are loaded into a lattice with 30% larger single-beam lattice depths than the final values used for the actual measurements. This suppresses resonant transfer of atoms to higher bands. The modulation amplitude is then linearly increased within 20 ms to reach a normalized drive of  $K_0 = 0.7778$ , where  $K_0 = \pi^2(A/\lambda)(\hbar\omega/E_R)$ , with  $A$  the amplitude of the motion,  $\omega/2\pi$  the modulation frequency and  $\hbar = \hbar/2\pi$ . The time-dependence of the lattice position  $\mathbf{r}_{\text{lat}}(t)$  is then given by

$$\mathbf{r}_{\text{lat}} = -A(\cos(\omega t)\mathbf{e}_x + \cos(\omega t - \varphi)\mathbf{e}_y) \quad (5)$$

where  $\mathbf{e}_x$  and  $\mathbf{e}_y$  denote the real-space unit vectors along the  $x$  and  $y$  directions. The phase  $\varphi$  is set with an accuracy of  $3^\circ$ . When using different modulation frequencies, we keep  $K_0$  constant. The lattice depths are then finally reduced to their final values within 10 ms. We have independently confirmed that the modulation frequency of  $\omega/2\pi = 4$  kHz exceeds the combined static bandwidth of the two lowest bands using lattice phase-modulation spectroscopy.

We have verified that our experimental findings are not affected by the global phase of the lattice modulation or changes in the total modulation time smaller than a modulation period. This means that a time-independent effective Hamiltonian can safely be used. Additionally, we have varied the timescale on which the modulation is ramped on and off to confirm that these ramps are sufficiently slow and the measurements are not affected by switch-on or switch-off effects.

**Detection.** After one Bloch cycle lasting 9.85 ms (8.72 ms) for  $x$  ( $y$ ) oscillations, the lattice modulation amplitude is linearly lowered to zero within 2 ms. The quasi-momentum distribution of the atoms is then probed using a band-mapping technique, where all lattice beams are ramped down within 500  $\mu\text{s}$ , which is much shorter than the timescales of the harmonic trap, meaning that the original  $\mathbf{q}$ -space distribution is conserved<sup>8</sup>. An absorption image of the atomic distribution is then recorded after 15 ms of ballistic expansion. The fraction of atoms per band is determined by integrating the atomic density in the corresponding Brillouin zone in the absorption image. The size of the Brillouin zone is independently calibrated by using Bloch oscillations of a non-interacting Fermi gas in a one-dimensional lattice. Owing to the residual non-adiabaticity of the lattice ramps, 16% (14%) of the atoms are detected in the second band and 21% (8%) in even higher bands after loading the lattice and before the Bloch cycle including (not including) the linear ramps of the modulation.

For the drift measurements, the displacement of the atoms with respect to the position before the Bloch oscillation is obtained by calculating the centre of mass within the first Brillouin zone. The differential drift is then calculated as the difference of the recorded drift for oscillations along the positive and negative  $q_y$  direction. We already observe individual drifts when only breaking IS, which constitutes a measurement of a local Berry curvature (see below and Extended Data Fig. 2). The drift depends strongly on the size of the energy gap, which supports our explanation for the precursors of the topological phase in Fig. 4.

**Effective band-structure calculations.** The effective Hamiltonian  $\hat{H}_{\text{eff}}$  is given by a logarithm of the time-evolution operator for one modulation period. Numerically, we discretize time and  $\mathbf{q}$ -space, choosing the grid such that a higher resolution does not further change the results. Analytically, we use a Magnus expansion in  $1/\omega$ . The energy spectrum, Berry curvature and Chern number are computed from  $\hat{H}_{\text{eff}}$  using the usual methods employed for static Hamiltonians. By comparing with numerical results and computing higher-order terms we show that the Magnus expansion can be truncated at first order in  $1/\omega$  for our parameters, and  $\hat{H}_{\text{eff}}$  then takes on the form of the Haldane Hamiltonian (equation (1)).

There,  $\mathcal{A}_{AB}$  is not affected by the modulation compared to the static lattice and  $t_{ij}$  are renormalized by a factor of about 0.85 with variations of  $\pm 0.03$ , depending on  $\varphi$  and the orientation of the tunnelling. The induced imaginary next-nearest-neighbour tunnelling takes on values of up to  $\hbar \times 18$  Hz for the diagonal links and  $\hbar \times 5$  Hz for the vertical links. Its value depends only on the modulation amplitude (scaling as a product of two second-order Bessel functions), the frequency (scaling as  $1/\omega$ ), and the product of two nearest-neighbour tunnel couplings which correspond to this next-nearest-neighbour tunnelling. Static real next-nearest neighbour tunnel couplings do not affect other terms in  $\hat{H}_{\text{eff}}$  and are not required to open a gap, meaning that our approach works equally well in deep optical lattices. The weights  $w_i$  determining the gap in equation (3) are 3.5 and 2.1 for the vertical and diagonal tunnel couplings respectively, with variations of about  $\pm 0.1$  as a function of  $\varphi$ . Detailed derivations, formulae for all terms in the effective Hamiltonian, and comparisons between numerical and analytical approaches can be found in the Supplementary Information.

**Semi-classical calculations.** We use a semi-classical approximation to simulate the orthogonal drifts observed for Bloch oscillations along the  $y$  direction in the experiment, using the same lattice parameters as in Fig. 2. We denote the energy and Berry curvature of the lowest band of the analytical effective Hamiltonian with  $\epsilon(q_x, q_y)$  and  $\Omega(q_x, q_y)$ . The external accelerating force is given by  $F_y = \pm 2\Delta E/\lambda$ , where  $\Delta E/\hbar = 114.6$  Hz is the energy offset per site. The equations of motion then read (omitting the  $z$ -direction, which de-couples)

$$\dot{x} = \frac{1}{\hbar} \partial_{q_x} \epsilon(q_x, q_y) - \dot{q}_y \cdot \Omega(q_x, q_y) \quad (6)$$

$$\dot{y} = \frac{1}{\hbar} \partial_{q_y} \epsilon(q_x, q_y) + \dot{q}_x \cdot \Omega(q_x, q_y) \quad (7)$$

$$\hbar \dot{q}_x = -\partial_x V_{\text{trap}}(x, y, z) \quad (8)$$

$$\hbar \dot{q}_y = F_y - \partial_y V_{\text{trap}}(x, y, z) \quad (9)$$

The effect of the harmonic trap is taken into account with  $V_{\text{trap}}(x, y, z) = 0.5m(\omega_x^2 x^2 + \omega_y^2 y^2 + \omega_z^2 z^2)$ .

As the underlying band structure possesses several symmetries, the possible values of the differential drift  $\mathcal{D}$  are strongly constrained by the topology of the lowest band. When only TRS (IS) is broken, the band structure is point-symmetric,  $\epsilon(q_x, q_y) = \epsilon(-q_x, -q_y)$ . Additionally, the Berry curvature is point-symmetric (point-antisymmetric), so the lowest band is topologically non-trivial (trivial). If the system is also reflection-symmetric,  $\epsilon(q_x, q_y) = \epsilon(-q_x, q_y)$ , the equation of motion for  $\dot{q}_x$  remains unchanged when inverting the direction of the force in the topologically trivial case. Thus, a differential drift can only appear if the lowest band is topologically non-trivial. In the experiment, these symmetries are strictly present when  $\varphi = \pm 90^\circ$ . The modulation weakly breaks reflection symmetry otherwise (see Supplementary Information) but it can be restored by considering the average of  $\mathcal{D}(\varphi)$  and  $\mathcal{D}(\pi - \varphi)$ . For both cases the experimental data of Figs 2d and 4c shows that the lowest band is topologically non-trivial.

For the numerical simulations, we compute  $4 \times 10^4$  trajectories, starting from a zero-temperature fermionic phase-space distribution (taking into account the  $z$ -direction) resembling the measured initial momentum-space distribution, and then determine the  $\mathbf{q}$ -space centre-of-mass position after one Bloch cycle. For a rough estimate of the effects of Landau-Zener transfers to the second band, we record the minimum bandgap experienced by each trajectory and exclude trajectories below a chosen cut-off value. This approach will not capture the complex quantum-mechanical dynamics of the real transfer process, but may serve to indicate in which direction the measured drift curves will be deformed.

Extended Data Fig. 1a shows that no differential drift is expected when only IS is broken, as observed in the experiment. In particular, even though reflection symmetry is weakly broken in the system as stated above, its effect remains smaller than the numerical error on  $\mathcal{D}$ . The simulations furthermore show that for each individual applied force a drift should appear, as observed (see below and Extended Data Fig. 2a). When only TRS is broken, a differential drift that changes sign with the modulation phase  $\varphi$  is computed, which is smaller but comparable to the measured values. The sudden change of  $\mathcal{D}$  around  $\varphi = 0^\circ$  is smoothed when taking into account transfer to higher bands. In that region the gap at the Dirac points and the spread of the Berry curvature is very small, meaning that the atoms which would contribute most to the drift are likely to be transferred to the higher band. A similar effect appears in Extended Data Fig. 1c, where both IS and TRS are broken for circular modulation. Without transfer, our simulations predict a sudden change in  $\mathcal{D}$  at the topological transition. When taking transfer into account, the Dirac point with the smaller gap contributes less, so the drifts observed in the topological regime extend beyond the transition line, as measured in the experiment (see Fig. 4a). This transfer could be reduced by applying weaker gradients to the atomic cloud, which would, however, require removing the harmonic trapping potential along the  $y$  direction.

The underlying harmonic trap in the  $x$  direction is also of particular importance, as it is responsible for transforming displacements in real space into momentum-space drifts. As seen in Extended Data Fig. 1d, the differential drift vanishes when  $\omega_x$  does, increases rapidly close to the experimental value of  $\omega_x = 2\pi \times 14.4(6)$  Hz and shows oscillatory behaviour when the timescale of dipole oscillations becomes comparable to the Bloch oscillation period.

**Drift measurements for opposite forces.** Now we discuss the individual drift observed after one full Bloch cycle supplementing Fig. 2c and d and Fig. 4 in the main text. Our measurement technique probes the Berry curvature of the lowest band by moving atoms in the  $q_y$  direction past the gapped Dirac points, where the Berry curvature is localized, and relies on the coupling of real and momentum space. Note that the width of the fermionic cloud is sufficiently large that by performing a Bloch oscillation we sample the entire Brillouin zone. As described in the main text, the applied uniform force causes an orthogonal velocity in real space when atoms are in the region of the Berry curvature. The resulting change in real space position induces a transverse force arising from the underlying harmonic confinement in the opposite direction to the direction of the displacement. As a result, we observe a drift in quasi-momentum, which is amplified by the negative effective mass at each Dirac point arising from the negative curvature of the band structure.

In the topologically trivial case, when only IS is broken, for each individual gradient we observe an equal drift along  $q_x$  when scanning the sublattice offset  $\Delta_{AB}$  (see Extended Data Fig. 2a). This constitutes a measure of the local Berry curvature, because the integrated Berry curvature is zero. We measure a drift which increases with increasing gap and changes sign with  $\Delta_{AB}$ . The data shows that the observed drift predominantly arises from the first Dirac point that is passed. This effect can be explained in the following way: The Berry curvature of the first Dirac point already leads to an orthogonal drift in quasi-momentum. When successively reaching the second Dirac point the shifted part of the cloud then does not experience the same Berry curvature distribution. As expected, opposite oscillation directions give rise to the same drift, since not only the direction of the force changes but also the sign of the Berry curvature corresponding to the first Dirac point on the trajectory (see

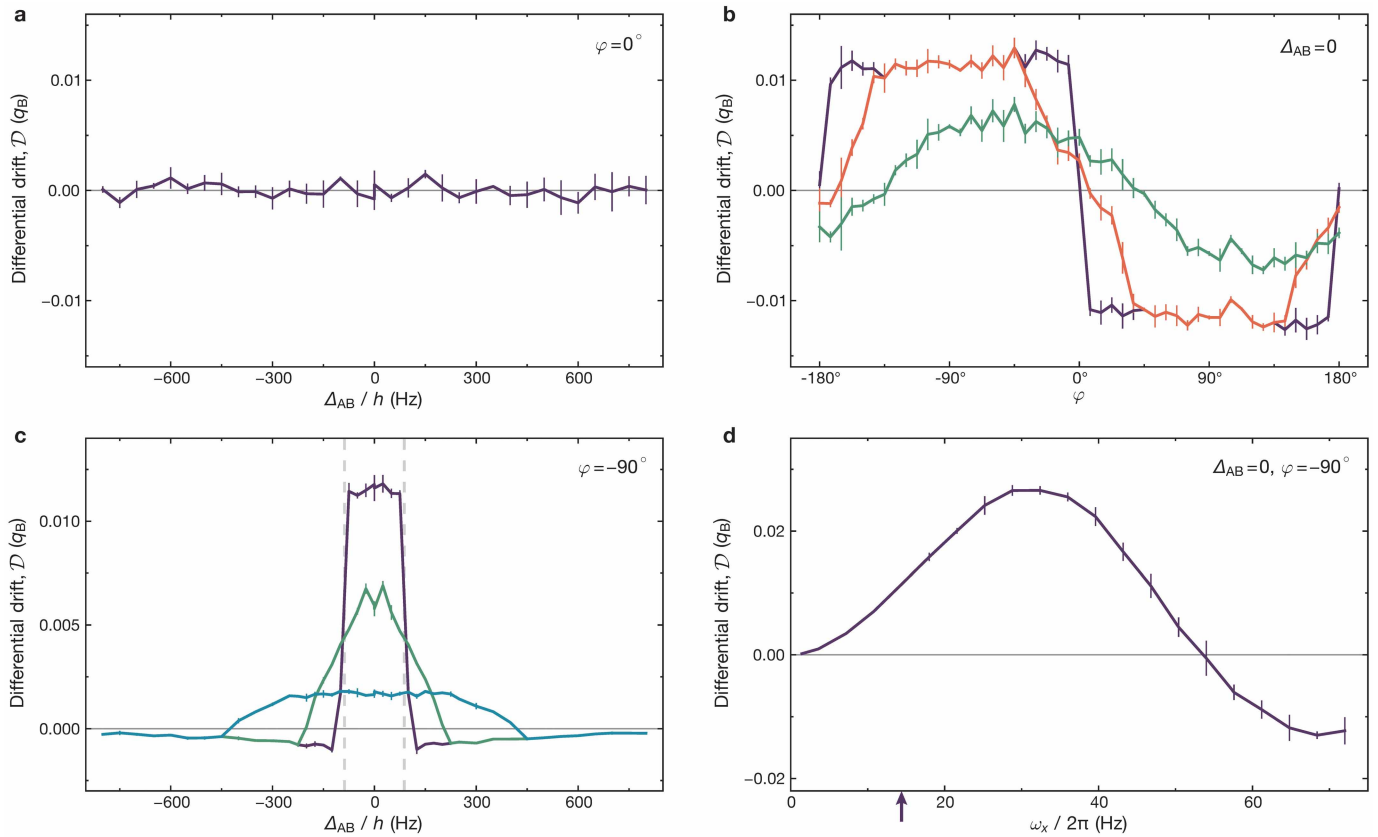
Extended Data Fig. 2). Subtracting the drifts of opposite gradients gives the differential drift  $\mathcal{D}$ , as shown in the main text. This probes the net contribution of both Dirac points. Only for the largest  $\Delta_{AB}$  does the measured drift decrease again, indicating an increasing spread of the Berry-curvature distributions at each Dirac point, which then start to overlap and gradually cancel each other. We also observe these drifts in a static lattice with  $\Delta_{AB} \neq 0$ .

In contrast, when only TRS is broken, we probe the topologically non-trivial regime. Extended Data Fig. 2b shows opposite drifts along  $q_x$  for each of the oscillation directions. In this case both successively passed Dirac points cause a drift in the same direction since the Berry curvature is point-symmetric. Therefore, changing the sign of the applied gradient leads to a drift in the opposite  $q_x$  direction. As expected, the drift changes sign for the opposite modulation phase difference  $\varphi$ , directly revealing the changing sign of the Berry curvature distribution. Here too, a larger gap (when  $\varphi$  is closer to  $\pm 90^\circ$  or the modulation frequency is lower) leads to a larger drift. The combination of the dependence of the drift on the size of the gap and the predominance of the first Dirac point on the trajectory may be the cause of the precursors seen in Fig. 4a for simultaneously broken IS and TRS.

**Heating of an interacting Fermi gas.** We have also investigated the increase in entropy in the modulated honeycomb lattice in comparison to the static case by loading a repulsively interacting Fermi gas into the lattice and reversing the loading procedure<sup>31</sup>. We prepare about  $2.0(2) \times 10^5$  atoms in a balanced spin mixture of the  $|F, m_F\rangle = |9/2, -9/2\rangle$  and  $|9/2, -5/2\rangle$  Zeeman states. The atoms are then loaded into a lattice with final depths  $V_{\bar{x}, \bar{y}, \bar{z}} = [14.0(4), 0.79(2), 6.45(20), 7.0(2)]E_R$  within 200 ms. This corresponds to a system consisting of coupled isotropic honeycomb layers with a nearest-neighbour tunnelling  $t/h = 172(20)$  Hz, as used in previous work<sup>27</sup>. The two lowest bands have a total bandwidth of  $h \times 1.0$  kHz, with a gap of  $h \times 14$  kHz to the next higher band (excluding the third direction). After turning on the lattice modulation (using the same  $K_0$  as in the main text, which opens a gap of about  $h \times 44$  Hz at the Dirac points), we reverse the loading procedure and measure the final temperature of the sample. This is compared to the case where the lattice is not modulated. From the difference in temperature before loading the lattice and after the procedure, the corresponding entropy increase can be determined. We measure the entropy increase for different interaction strengths and modulation frequencies. In the Mott-insulating regime with  $U/h = 4.18(2)$  kHz ( $U/5t = 4.9(6)$ ) and for a frequency of  $\omega/2\pi = 1.08$  kHz (which is the same in proportion to the bandwidth as in the measurements of the main text) we find an entropy increase that is 25% larger when modulating the lattice compared to the situation without modulation; see Extended Data Fig. 3a. In the crossover regime at  $U/h = 2.19(5)$  kHz ( $U/5t = 2.5(3)$ ) we find the same final entropy. This now corresponds to a 40% increase, which possibly originates from the creation of low-energy charge excitations for these parameters. In the measurements versus frequency, we cover the doublon excitation peak in the insulating phase, whose frequency is given by  $U/h = 4.18(2)$  kHz. We have furthermore measured the additional heating induced by holding the atoms in the modulated lattice for longer times; see Extended Data Fig. 3b. For all parameters we find a linear increase of entropy with time. For timescales relevant for studying dynamics, as in the measurements of the main text, this contribution is much smaller than the one associated with the modulation ramp. We find that the heating induced by the modulation does not dominate the final temperature, thus demonstrating that the scheme is well suited for studying many-body states in topological lattices.

**Proposal for creating spin-dependent Hamiltonians.** To realize spin-dependent Hamiltonians—for example, the Kane–Mele model—we propose to use an oscillating magnetic gradient in order to apply an oscillating spin-dependent force on the atoms. For the  $|9/2, -9/2\rangle$  state of  $^{40}\text{K}$ , maximum gradients of about  $10 \text{ G cm}^{-1}$  would be required to achieve the same  $K_0$  as in the main text when modulating with a frequency of 1 kHz. Owing to the Zeeman effect, another spin component or atomic species would experience a different force. If the magnetic moment of the second component is chosen to be opposite, the Kane–Mele model is simply realized by replacing one oscillating mirror in the experiment with this oscillating gradient. The two spin components would then experience clockwise or anti-clockwise modulated forces, respectively, and therefore the two spin bands would have opposite Chern numbers. In general, a combination of an oscillating mirror and magnetic gradient can be used to create the desired average and differential force for other combinations of magnetic moments. This approach can be extended to bosonic atoms or Bose–Fermi mixtures and is also suitable for creating other types of spin-dependent tunnelling, for example, situations where one species is pinned to the lattice and the other remains itinerant.

31. Greif, D., Tarruell, L., Uehlinger, T., Jördens, R. & Esslinger, T. Probing nearest-neighbor correlations of ultracold fermions in an optical lattice. *Phys. Rev. Lett.* **106**, 145302 (2011).

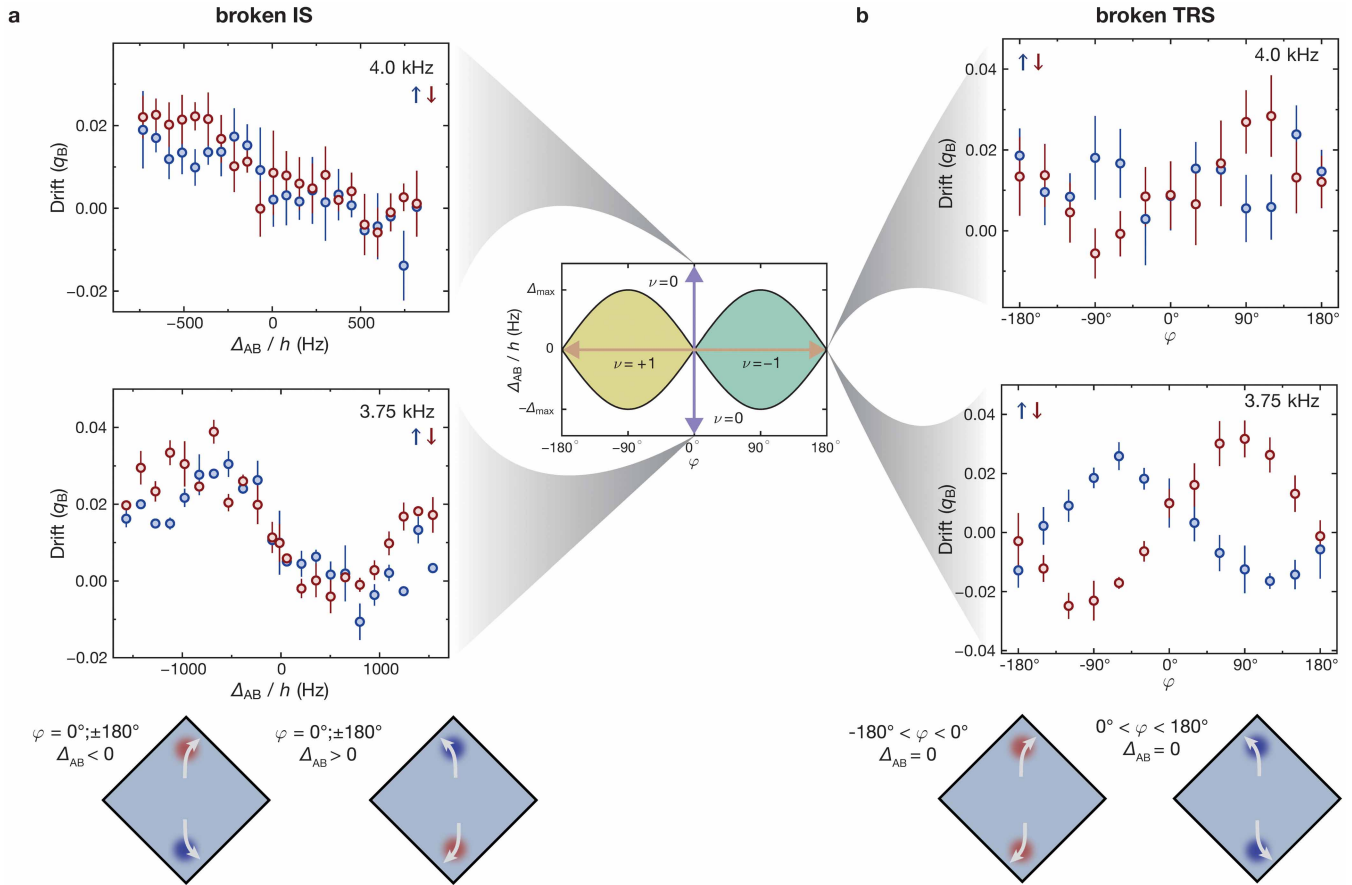


### Extended Data Figure 1 | Semi-classical simulations of the atomic motion.

The experiments shown in the main text in Fig. 2c and d are simulated using the semi-classical equations of motion (equations (6)–(9)). The band structure and the Berry curvature are those of the effective Haldane Hamiltonian (equation (1)). The atomic ensemble is modelled by a zero-temperature Fermi distribution. Data are mean  $\pm$  s.d. of three simulations containing  $4 \times 10^4$  trajectories. The differential drift  $\mathcal{D}$  is computed when breaking either IS (a) or TRS (b). The former shows no differential drift, in agreement with the experimental data of Fig. 2c. For the latter, the different curves take into account the transfer to the higher band by excluding trajectories passing through regions where the bandgap lies below a certain threshold. If this transfer is not taken into account (purple line), the differential drift varies sharply around  $\varphi = 0^\circ$  where the Chern number changes. However, as the threshold is raised to

$0.5\Delta E$  (red line) and  $\Delta E$  (green line) where  $\Delta E/h = 114.6$  Hz is the energy offset per site driving the Bloch oscillation, this sharp feature progressively smoothens and qualitatively reproduces the experimental measurements. c, When TRS is maximally broken ( $\varphi = 90^\circ$ ) and  $\Delta_{AB}$  varies, the transfer is also responsible for the differential drift extending beyond the topological phase. Without any transfer (purple line), the differential drift changes sharply around the topological phase transition (vertical dashed line), while it extends significantly in the topologically trivial phase when the threshold is set at  $\Delta E$  (green line) or  $3\Delta E$  (blue line). d, Influence of the transverse trapping frequency  $\omega_x/2\pi$ . The frequency used in the experiment is indicated by a purple arrow. For much larger frequencies the differential drift can vanish, as the transverse oscillation time becomes comparable to the Bloch period.

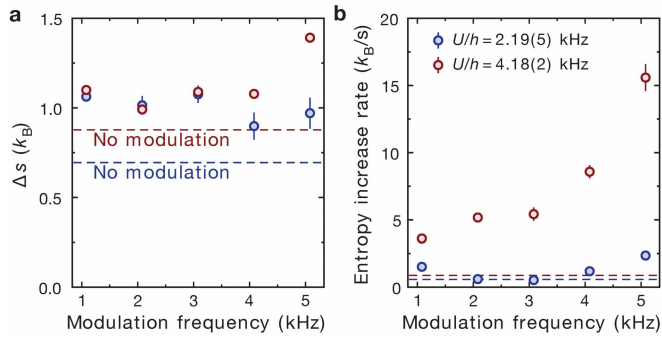




**Extended Data Figure 2 | Drift measurement for broken IS and TRS.** The measured drift used to obtain the differential drift  $\mathcal{D}$  in Figs 2c, d and 4 of the main text is individually shown for positive and negative forces in the  $q_y$  direction. Data for positive (negative) force is shown in blue (red). The central plot, showing the Haldane phase diagram, indicates the region which is scanned when breaking either IS (purple arrow) or TRS (brown arrow) in our system. **a**, We break IS by introducing a sublattice offset and show measurements with modulation frequency of 4.0 kHz and 3.75 kHz. Although the opposite Berry curvatures at the two Dirac points sum up to zero within the first Brillouin zone, we clearly see a drift depending on the size of  $\Delta_{AB}$ . Data show mean  $\pm$  s.d. of at least 6 (4.0 kHz) or 2 (3.75 kHz) measurements. **b**, By changing the modulation phase difference  $\varphi$  we break TRS and the system

enters the topologically non-trivial regime. Drift data for positive (negative) force is shown in blue (red) for a modulation frequency of 4.0 kHz and 3.75 kHz. Data show mean  $\pm$  s.d. of at least 21 (4.0 kHz) or 6 (3.75 kHz) measurements. Schematics below show the expected orthogonal drifts caused by driving the atoms through the Berry curvature distribution. Red (blue) indicates positive (negative) Berry curvature. If only IS is broken (**a**) the Berry curvature distribution is point-antisymmetric and changes sign when changing the sign of the sublattice offset. For opposite forces this leads to the same direction of the drift, as indicated by the white arrows. If only TRS is broken (**b**) the Berry curvature distribution at each Dirac point has the same sign, which is changed when reversing the rotation direction. In this case the opposite forces lead to opposite directions of the drift.





**Extended Data Figure 3 | Heating of a repulsively interacting Fermi gas.**

**a**, Entropy increase associated with loading into the modulated lattice and reversing the loading procedure. **b**, Entropy increase rate in the modulated lattice for long holding times. The modulation frequency  $\omega = 2\pi \times 1,080$  Hz opens a gap of  $h \times 44$  Hz in the non-interacting band-structure. This value, in units of the tunnelling, is similar to the measurements of the main text. The dashed lines show the measured heating in a lattice without modulation with identical interaction strengths.